J Nanopart Res (2012) 14:969
DOI 10.1007/s11051-012-0969-3

RESEARCH PAPER

Gram-scale synthesis of highly crystalline, 0-D and 1-D SnO_2 nanostructures through surfactant-free hydrothermal process

Umapada Pal · Mou Pal · Raul Sánchez Zeferino

Received: 17 February 2012 / Accepted: 30 May 2012 / Published online: 17 June 2012
© Springer Science+Business Media B.V. 2012

Abstract We report the synthesis of highly crystalline SnO_2 nanoparticle and nanorod structures with average diameters well within quantum confinement limit (3.5−6.4 nm), through surfactant-free hydrothermal synthesis. The size and shape of the nanostructures could be controlled by controlling the pH (4.5–13.0) of the reaction mixture and the temperature of hydrothermal treatment. Probable mechanisms for the variation of particle size and growth of one-dimensional structures are presented considering the size-dependent crystal solubility at lower pH values of the reaction solution and Ostwald ripening of the quasi-spherical nanoparticles at higher pH values, respectively. Variation of optical band gap energy and hence the effects of quantum confinement in the nanostructures have been studied.

Keywords SnO_2 nanoparticles and nanorods · Large-scale synthesis · Quantum confinement · Hydrothermal growth · Optical properties

Introduction

Current enhanced interest on the synthesis of semiconducting metal oxides nanostructures is primarily driven by their unique optical, chemical, and electrical properties. Among the common metal oxides, SnO_2, an *n*-type semiconductor with a wide band gap ($E_g = 3.6$ eV, at 300 K), large excitonic binding energy (130 meV), and a low electron affinity (Bhise et al. 2007), has been thoroughly investigated for various technological applications such as gas sensors for environmental monitoring (Xu et al. 2005; Mädler et al. 2006; Carreño et al. 2009), optoelectronic devices (Lee et al. 2004), transparent conducting electrodes (Sugimoto et al. 2004), catalyst supports (Jiang et al. 2004), energy storage (lithium batteries) (de Monredon et al. 2002), and energy conversion (Zhang and Gao 2004). The improved performance of SnO_2 nanostructures in such applications is primarily attributed to their large surface to volume ratio and the size-dependent electronic or optical properties. A variety of methods have been employed to prepare SnO_2 nanocrystals of different morphologies, such as hydrothermal (Chiu and Yeh 2007), thermal evaporation (Pan et al. 2001), microemulsion process (Liu et al. 2001a), chemical deposition (Liu et al. 2001b), solid state reactions (Xu et al. 2002; Sun et al. 2006), sol–gel (Broussous et al. 2002), sonochemical (Pang et al. 2001), among others. Ba et al. (2005) have developed the technique to synthesize highly uniform crystalline SnO_2 nanoparticles of 3.5 nm average diameter through a non-aqueous benzyl alcohol route. Shao et al. (2005) could synthesize hollow SnO_2 micro spheres through a template-free hydrothermal route. Nanowires, nanoribbons, and nanotubes of rutile and

U. Pal (✉) · M. Pal · R. S. Zeferino
Instituto de Física, Benemérita Universidad Autónoma de Puebla, Apdo. Postal J-48, 72570 Puebla, Puebla, Mexico
e-mail: upal@sirio.ifuap.buap.mx

orthorhombic tin oxide nanostructures have also been synthesized by Dai et al. (2002) using an elevated temperature synthesis technique (~1,100 °C). On the other hand, Cai et al. (2005) have fabricated asterisk-like SnO_2 nanostructures with multi-armed nanoribbons and nanowires by thermal evaporation of the mixture of SnO and Sn powders. However, reports on the synthesis of SnO_2 nanostructures of controlled morphology in the quantum confinement regime are scarce (Cheng et al. 2004). While solution-based techniques for the fabrication of nanostructures are considered promising due to their potentials for controlling their size and morphology and hence their physical properties (Alivisatos 1996; Hyeon et al. 2002), fabrication of anisotropic nanostructures through solution-based technique, specially without using organic ligands or surfactants, is of great importance as the inherent physical properties of the nanostructures can be preserved.

In this article, we report on the synthesis of highly crystalline quantum confined zero-dimensional (0-D) and one-dimensional (1-D) SnO_2 nanostructures through a ligand or surfactant-free hydrothermal method at relatively low temperatures. The low-temperature hydrothermal synthesis route is a superior alternative to the post-growth calcination process needed for the crystallization of SnO_2 prepared by other methods (Wang et al. 2003). Effects of solution pH and temperature of hydrothermal treatment on the size and morphology control of the nanostructures have been discussed.

Experimental

A typical synthesis process started with the preparation of aqueous solutions of $SnCl_4{\cdot}5H_2O$ (5.0 mmol/1.753 g) and NaOH (22.2 mmol/0.89 g) by dissolving them in 10.0 and 20.0 mL of deionized (DI) water, respectively. Subsequently, the NaOH solution was slowly added to $SnCl_4$ solution drop-wise under magnetic stirring to adjust the pH of the mixture solution to a desired value. Then 30.0 mL of anhydrous ethanol was added to the above mixture. Different solutions were prepared with final pH values maintaining at 5, 7, 9, 11, or 13. To prepare the reaction solutions of pH 11 and 13, a NaOH solution of higher concentration was utilized. The pale-white turbid mixture was transferred into a Teflon-lined stainless steel autoclave and treated hydrothermally either at 180 or 225 °C for 12 or 24 h. After the hydrothermal treatment, the autoclave was passively cooled down to room temperature, and the white precipitate formed at the bottom was collected, separated by centrifuging (8,000 rpm, 20 min.), washed repeatedly with water and ethanol, and dried at 80 °C in air for several hours. Powder samples of the order of gram amount were obtained. To check the morphology and size reproducibility of the grown nanostructures, synthesis of each sample was repeated at least three times.

Structural analyses of the powder samples were carried out through X-ray diffraction (XRD) and transmission electron microscopy (TEM) using a Siemens D8 Discover diffractometer (Cu K_α source; $\lambda = 1.5406$ Å, accelerating voltage = 25 keV, filament current = 40 mA, scanning range $2\theta = 10$–$75°$, step size = 0.02°, dwell time = 1 h) and a JEOL FEG 2010F FasTem electron microscope (operating at 200 keV), respectively. Optical properties of the nanostructures were evaluated by Raman spectroscopy, diffused reflectance in the UV–vis spectral range, Fourier transform infrared (FTIR) spectroscopy, and photoluminescence (PL) spectroscopy at room temperature. FTIR analysis of the samples was performed using a Nicolet Magna 750 spectrometer in the 4,000–400 cm^{-1} spectral range. Diffused reflectance spectra (DRS) of the samples were recorded in the 200–800 nm range using a Varian Cary 5000 spectrophotometer attached with an integrating sphere. A Perkin–Elmer NIR Spectrum GX FT-Raman spectrometer with Nd:YAG laser source (1,064 nm, 500 mW) was used for recording the Raman spectra at room temperature. The PL spectra of the SnO_2 samples were recorded by a 1-m long ScienceTech monochromator using a Hamamatsu PMH-04 photomultiplier and a He-Cd laser (as excitation source, $\lambda = 325$ nm).

Results and discussion

The structural phase and crystallinity of the SnO_2 nanostructures obtained at different pH values were tested through their XRD patterns (Fig. 1). There appeared well-defined intense XRD peaks for all the samples, and the diffraction peaks matched well with the tetragonal rutile phase of SnO_2 (JCPDS file # 88-0287). As can be appreciated from Fig. 1, intensity of the diffraction peaks increases with the increase of

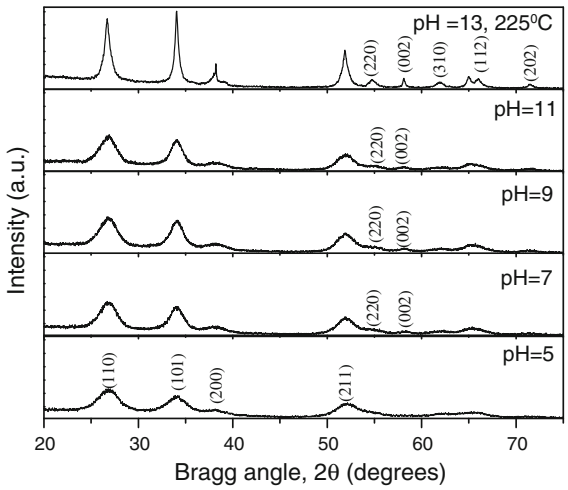

Fig. 1 X-ray diffraction patterns of SnO_2 nanostructures grown at different pH values. All the samples were prepared with hydrothermal treatment at 180 °C for 12 h, except the sample prepared with pH 13 (225 °C, 24 h)

pH value of the reaction mixture, indicating an improvement of crystallinity at higher pH values. However, the XRD peaks are quite broad due to small particle size of the samples. While the increase of solution pH causes a gradual increase in diffraction peak intensity, the increase is drastic when the temperature of hydrothermal treatment increased from 180 to 225 °C, specially for higher pH values of the reaction mixtures.

Figure 2 shows typical low-resolution TEM images of SnO_2 nanostructures grown at different pH values. Formation of ultrafine, highly monodisperse, quasi-spherical SnO_2 particles is observed for the pH values 5–7. On further increasing the pH to 9, the particles tend to agglomerate to some extent and become slightly elongated in shape. For a fixed temperature of hydrothermal treatment (180 °C), the average size of the SnO_2 nanoparticles first decreases with the increase of pH and then increases beyond pH 8. At pH 11, even for 180 °C temperature of hydrothermal treatment, the spherical morphology of the nanoparticles changes to rod-like morphology (Fig. 2d). The tendency of forming elongated nanostructures is pronounced for the pH values higher than 9.0. On increasing the pH of the reaction mixture to 13, even for the hydrothermal treatment at 180 °C resulted in 100 % conversion of nanoparticles to rod-like elongated structures of relatively low-aspect ratio (length/diameter ~ 2.8; not shown). Finally at pH 13 and 225 °C hydrothermal temperature, uniform nanorods with average diameter of 5.8 nm and length up to 68.0 nm are produced (aspect ratio ~12). The diameters of the nanorods are very much similar to that of the primary nanoparticles (the particles grown at lower pH values), which suggests that the rod-like anisotropic nanostructures might have been produced from the initially formed spherical nanoparticles in the hydrothermal reactions (Gu et al. 2004). Dimensions of the nanostructures were measured from their high-resolution transmission electron microscopic (HRTEM) images, and their size distribution histograms are presented as insets of Fig. 2. The relationship between the pH value of the reaction mixture and the average size of the produced particles is displayed in Fig. 3. It can be seen that the average diameter of the particles first decreases from 5.4 to 3.5 nm on increasing the pH value from 5 to 7 and then increases up to 5.6 nm when the pH increased up to 11. The change in average size of the spherical particles can be understood considering the size-dependent crystal solubility described by Thompson–Freundlich equation (Lifshitz and Slyozov 1961). In a supersaturated aqueous medium, the tiny crystalline nuclei are formed, which followed by their growth (Yu et al. 2003). When most of the excess solute gets precipitated in a supersaturated solution during the reaction (hydrolysis in this case) process, there is a considerable decrease in saturation level. Under such condition, the smaller particles begin to dissolve and the larger particles grow by consuming the smaller ones. This process is commonly known as Ostwald ripening and is a common growth mechanism for several metal oxide nanostructures produced by bottom-up approach. The driving force in Ostwald ripening arises because the concentration of solute in the vicinity of small particles is higher than the average supersaturation, while it is lower in the vicinity of larger particles (Jain and Hughes 1978). It is worth mentioning that the growth by Ostwald ripening usually produces spherical-shaped particles, which is thermodynamically most stable due to minimization of overall surface energy. We speculate that in our case, the spherical particles were formed at lower pH values through the assembly of tiny crystallites with rapid crystal growth at a relatively high degree of supersaturation (Lee et al. 2006). At pH 7, the primary nanocrystals undergo dissolution, resulting in the formation of smaller particles. With further increase

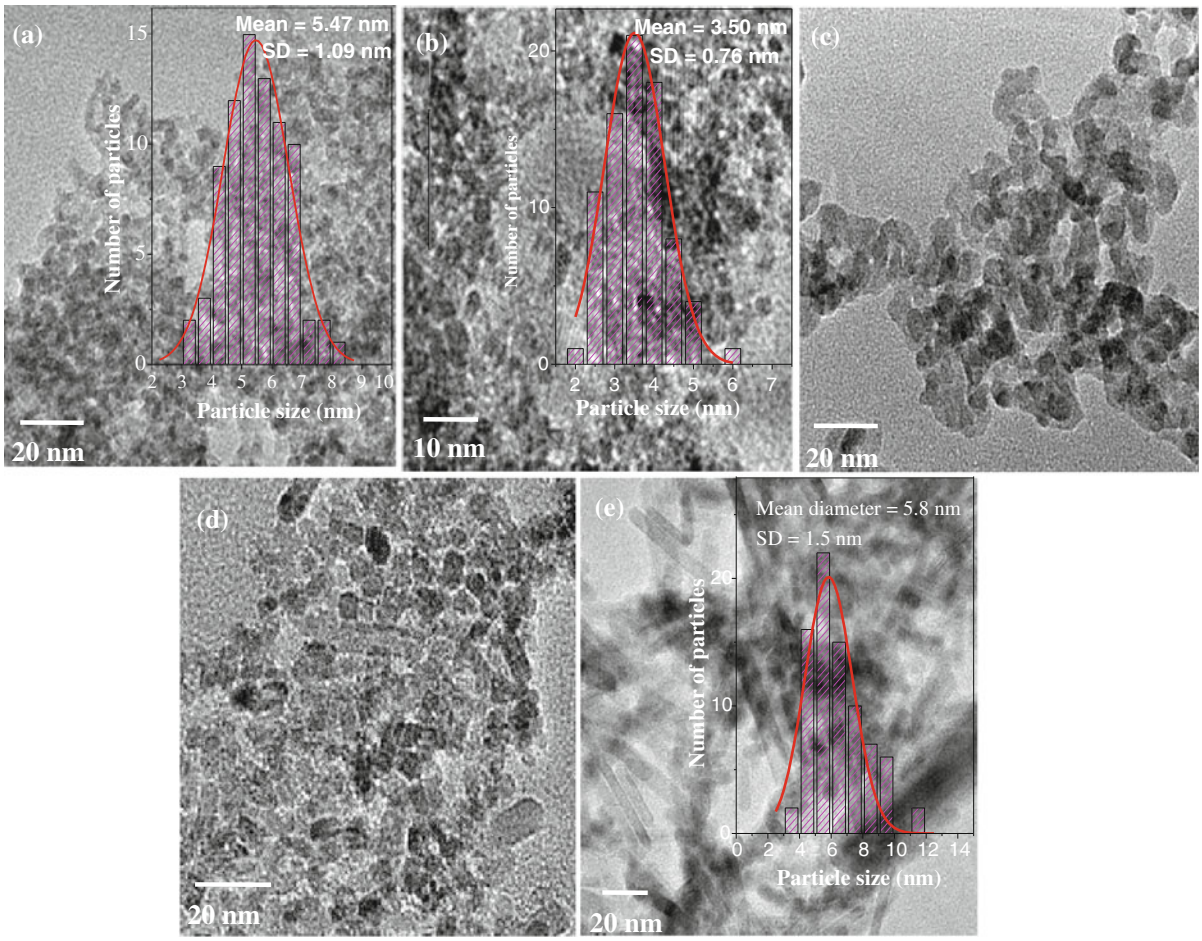

Fig. 2 Typical TEM micrographs of the SnO_2 nanoparticles grown hydrothermally at: **a** pH 5/180 °C/12 h, **b** pH 7/180 °C/12 h, **c** pH 9/180 °C/12 h, **d** pH 11/180 °C/12 h, and **e** pH 13/225 °C/24 h. Particle size distribution histograms of the samples are presented as *insets*

of pH, such particles grow in size as they incorporate more grains/growth units that they encounter in the reaction medium. Previous results reported by Jiang et al. (2005) have also shown the suppression of particle growth in the pH range 2–6 (inset of Fig. 3), but above pH 7 they did not observe the formation of particles. The distinct results of these two experiments may be attributed to the used alcohol which was ethylene glycol instead of ethanol, mixing ratio of alcohol to water, and the nature of initial precursor salt, tin (II) halide instead of tin (IV) halide which we used in our experiment. It is very clear from Fig. 2d that at pH 11, the nanoparticles have the tendency to grow along certain crystallographic direction and the complete evolution of morphology from spherical to anisotropic nanostructure (1-D) occurs at pH 13.

The HRTEM images presented in Fig. 4 clearly show a morphological evolution of the nanostructures grown at different pH values. The lattice fringes with spacing of 0.33 nm correspond to the (110) plane of rutile SnO_2. It is important to note that these 1-D SnO_2 nanostructures grow preferentially along [001] direction. To understand this preferential growth behavior, we must consider the surface energies of SnO_2 in different crystallographic orientations. The theoretical calculations made by several groups (Slater et al. 1999; Leite et al. 2003) revealed the same general trends: in order of increasing energy, the surfaces follow the sequence (110) < (100) < (101) < (001). Since (110) surfaces are suggested to have the lowest surface energy, the growth along [110] direction is highly unfavored. The preferential growth along [001]

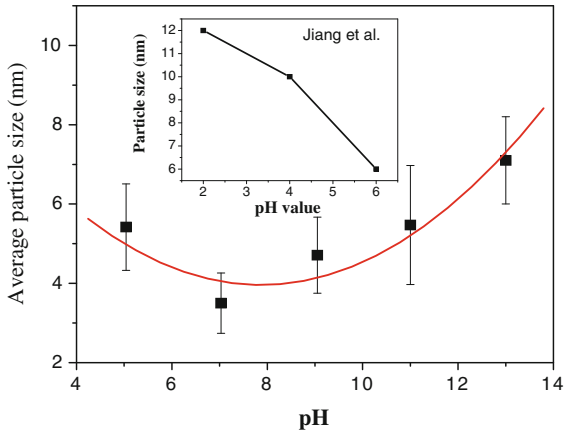

Fig. 3 Variation of average particle size on the pH value of the reaction mixture. The variation reported by Jiang et al. (2005) has been shown as *inset*. The *smooth red line* is the computer fitted curve to the experimental data points, and the *vertical bars* at the experimental data points represent the distribution widths

direction in the present case (Fig. 4e) provides a strong evidence that the growth of the rod-like 1-D structures occurs neither by monomer deposition nor by particle coarsening, but only through a coalescence mechanism, i.e., oriented attachment. This anisotropic alignment is attained by restricting the attachment process in some crystallographic directions and is the dominant mechanism in the formation of anisotropic structures of nanomaterials. By analyzing the morphology and size of the SnO_2 nanostructures grown at different pH values, we suggest that at lower pH values (pH < 11), the growth event occurs through Ostwald ripening and the particles do not undergo oriented attachment process. At pH > 11, solubility of SnO_2 in the reaction solution is extremely low, and hence, the coarsening process is insignificant. Under such reaction condition, oriented attachment of spherical nanoparticles formed in the reaction mixture is favored, and the 1-D nanostructures of uniform diameter are produced.

For evaluating the band gap energy, DRS spectra of the SnO_2 nanostructures were treated with the Kubelka–Munk relation (Kubelka and Munk 1931; Escobedo-Morales et al. 2007). Band gap energies of the samples were estimated from the variation of Kubelka–Munk function $F(R_\infty)$ (also known as remission function) with photon energy (Fig. 5). As can be seen, the band gap energy of the nanostructures first increases with the increase of pH of the reaction mixture and then decreases in accordance with the variation of their particle size (see the inset of Fig. 5). As can be appreciated, the DRS estimated band gaps of all the samples are much higher than the band gap energy of bulk SnO_2 (3.6 eV), confirming the quantum confinement of charge carriers in the nanostructures. Effective band gap of the nanostructures were also calculated using the effective mass approximation relation (Xu et al. 2008):

$$E_g^{\text{eff}} = E_g + \frac{\hbar^2\pi^2}{2\mu R^2} - \frac{1.8e^2}{4\pi\varepsilon_0\varepsilon R} + \text{small terms}, \qquad (1)$$

where E_g is the bulk band gap energy, R is the nanocrystal radius (average radius of the nanoparticles estimated from their TEM micrographs in the present case), $\hbar$ is Plank's constant divided by 2π, and μ is the effective reduced mass. The dielectric constant $\varepsilon = 14$ and reduced mass $\mu \approx m_s^* = 0.275m_s$ (because $m_s^* \ll m_h^*$ where m_s^* and m_h^* are the effective masses of electron and hole, respectively) of bulk SnO_2 were considered for calculations. Surprisingly, the calculated band gaps of the nanostructures were considerably (9–15 %) smaller than their values estimated from DRS analysis (see the inset of Fig. 5). To understand this discrepancy, we estimated the average grain size of the samples from their XRD patterns using Scherrer relation and found that the average grain size of the nanoparticles (samples prepared at pH values 5–11) is $\sim$10 % lower than their TEM estimated values. However, the argument cannot be applied for the sample prepared at pH 13 and hydrothermal treatment at 225 °C, as the nanostructures are 1-D and perfect single crystalline in nature. A careful observation of the HRTEM images presented in Fig. 4 would reveal that the 1-D structures are not uniform in diameter; rather, they are sheet-like with thickness less than 3.0 nm. Therefore, the quantum confinement effect is stronger along their thickness. In fact, even the apparent spherical nanoparticles produced at lower pH values might be the round-shaped sheet-like structures. The observed blue-shift in the effective band gap of these nanostructures probably the result of combined effects (quantum confinement) of their width and thickness which cannot be distinguished in the diffuse reflectance spectra of the powder samples.

In order to study the effect of pH on the Raman scattering of hydrothermally grown SnO_2 nanoparticles, room temperature Raman spectra of all the

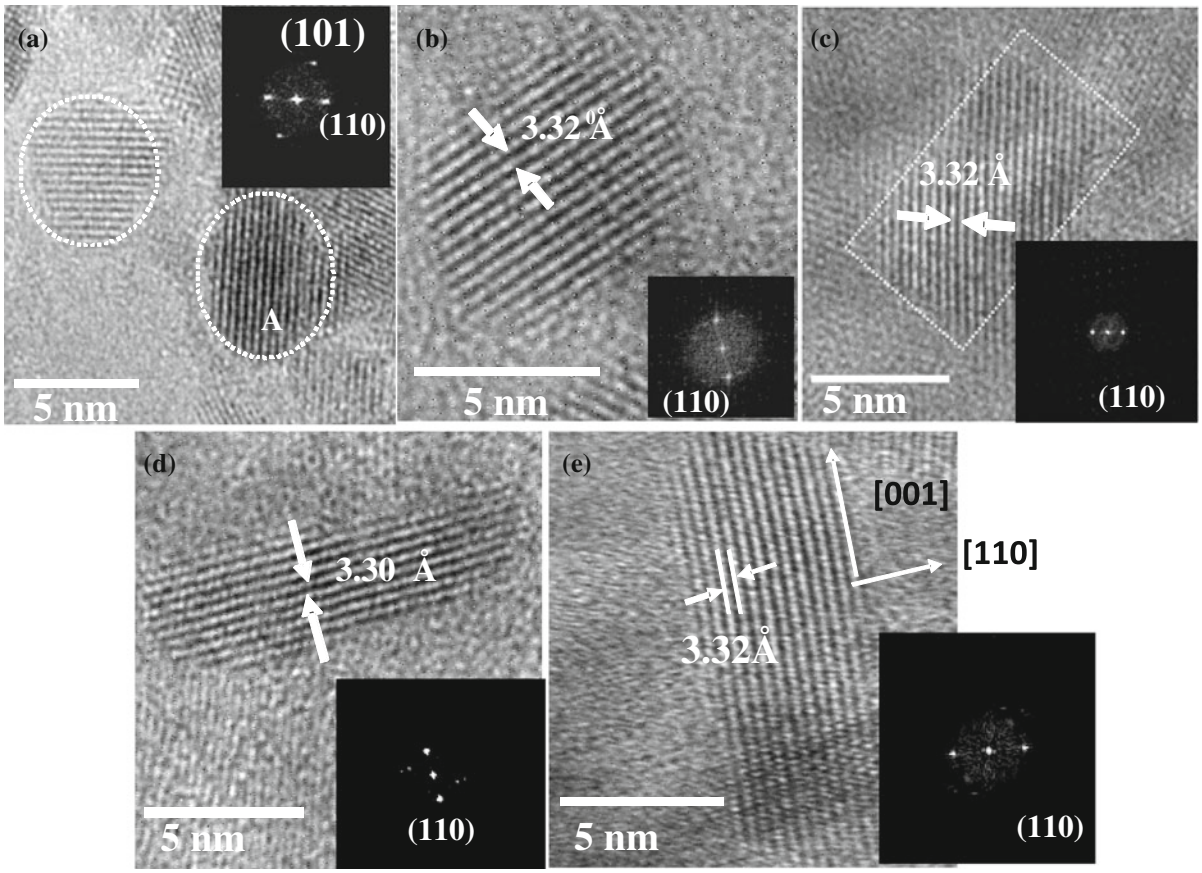

Fig. 4 Typical HRTEM images of SnO_2 nanoparticles grown at: **a** pH 5/180 °C/12 h, **b** pH 7/180 °C/12 h, **c** pH 9/180 °C/12 h, **d** pH 11/180 °C/12 h, and **e** pH 13/225 °C/24 h. *Insets* show the fast Fourier transform of a selected area for each SnO_2 sample

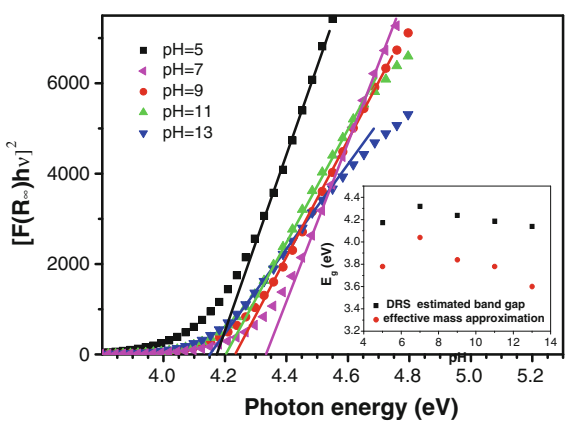

Fig. 5 Kubelka−Munk-treated DRS spectra of the SnO_2 nanostructures prepared at different pH values. *Inset* shows the variations of band gap energy with pH values estimated from DRS analysis and calculated using effective mass approximation

samples was measured. For SnO_2, the six unit cell atoms give rise to the following 18 vibrational modes at the Γ point of the Brillouin zone (Merle et al. 1980; Dieguez et al. 2001):

$$\Gamma = A_{1g} + A_{2g} + B_{1g} + B_{2g} + E_g + 2A_{2u} + 2B_{1u} + 4E_u \quad (2)$$

Of these 18 modes, two are IR active (the singe A_{2u} and the triply degenerate E_u), four are Raman active (three non-degenerate modes, A_{1g}, B_{1g}, B_{2g}, and the doubly degenerate E_g), and two are silent (A_{2g} and B_{1u}). One A_{2u} and two E_u modes are acoustic (Zhou et al. 2006).

Figure 6 shows the Raman spectra of the SnO_2 nanostructures grown at different pH values in the spectral range 400–800 cm^{-1}. The Raman scattering peaks appeared at about 482, 635, and 778 cm^{-1} are associated with the fundamental E_g, A_{1g}, and B_{2g}

modes of rutile SnO_2, respectively, confirming the growth of SnO_2 nanostructures in pure phase (Chen et al. 2006; Hu et al. 2002). Among these classical modes, B_{2g} is most sensitive to the particle size and shifts toward lower wave numbers as the size decreases. Two Raman bands at 543 and 584 cm^{-1} appeared as a consequence of disorder activation. The intensity and position of these bands depend on the nanoparticle size (Dieguez et al. 2001). It can be seen that the synthesis of SnO_2 at lower pH values induces a broadening and an intensity reduction of the principal modes, which could be related to the effects of nanometer size and internal strain produced during lattice growth at lower pH values. With the variation of pH of the reaction mixture, the intensity and width of the 584 cm^{-1} silent mode varied in accordance with the variation of particle size, i.e., on decreasing particle size, the intensity of the band decreased and became broader, as has been observed by Dieguez et al. (2001). However, the other silent mode (543 cm^{-1}), which was almost unrecognizable for the spherical or quasi-spherical nanoparticles fabricated at 180 °C hydrothermal treatment, became very much intense for the sample prepared at pH 13 and 225 °C. Though the origin of this silent mode is associated to the breakdown of long-range crystal symmetry in nanocrystals with high surface area and other surface imperfections, a high contribution of this mode in the Raman spectra of crystalline nanocrystals as in the present case is not expected. As has been described by Dieguez et al. (2001), the surface of otherwise highly crystalline nanoparticles has interfacial component consisting of grain boundary atoms or surface atoms. The surface atoms, which may constitute several atomic layers, are frequently displaced from their exact positions required to form ideal crystalline structure. Surface reconstruction in the (110) plane of single-crystalline SnO_2 involving up to three atomic layers and the presence of oxygen vacancies have also been demonstrated by Jones et al. (1997). Therefore, non-stoichiometry and lattice disorder at the nanocrystal surface generate the silent modes in small SnO_2 nanoparticles. As has been discussed earlier, our 1-D SnO_2 nanostructures fabricated at pH 13.0 and at 225 °C hydrothermal treatment are planer in nature with considerably smaller thickness than their widths. Presence of a high density of surface atoms is expected in such planer structures, which are disorder in nature, containing oxygen

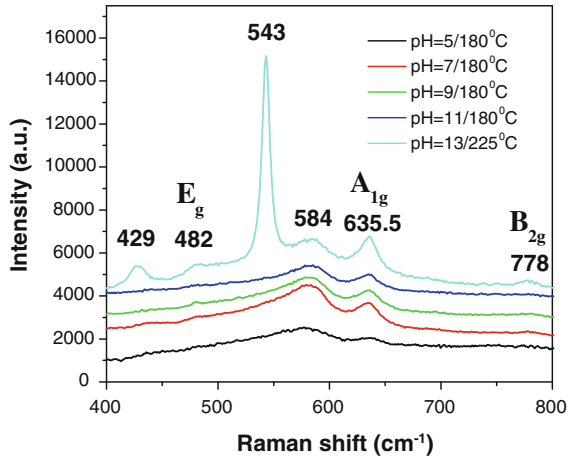

Fig. 6 Raman spectra of the SnO_2 nanostructures grown at different pH values

vacancies, inducing an intense surface mode as we can see in the Fig. 6. In fact, appearance of this silent mode in nanostructured SnO_2 has also been associated with the surface bound atoms by Sangeetha et al. (2011). The origin of Raman scattering peak at 429 cm^{-1} for the sample grown at pH 13 is not clear at this moment.

Fourier transform infrared spectra of all the samples revealed similar features. In Fig. 7a, a typical FTIR absorption spectrum of the SnO_2 nanoparticles is shown. The absorption peaks around 1,634 and 3,432 cm^{-1} appeared due to bending and stretching vibrations of water molecules absorbed at the surface of tin oxide, respectively. Two strong peaks appeared around 526 and 662 cm^{-1} belong to O–Sn–O and Sn–O stretching vibrations, respectively, suggesting the well-crystalline nature of the SnO_2 nanostructures (Shen et al. 2004). A shoulder peak appeared around 568 cm^{-1} is associated with the antisymmetric Sn–O–Sn stretching vibration of the surface bridging oxide formed through condensation of adjacent surface –OH groups (Chen and Gao 2004). The bands appeared in the 850–1,357 cm^{-1} range are associated to the bending modes of different types of surface terminated –OH groups (Zhang et al. 2011). The peak appeared at around 2,354 cm^{-1} belongs to residual CO_2 traces in the atmosphere of the spectrometer.

Similar to the FTIR spectra, room temperature PL spectra of the samples revealed identical features. As can be seen from the typical PL spectrum presented in Fig. 7b, there appeared two prominent emissions at about 414 and 436 nm, correspond to 2.99 and

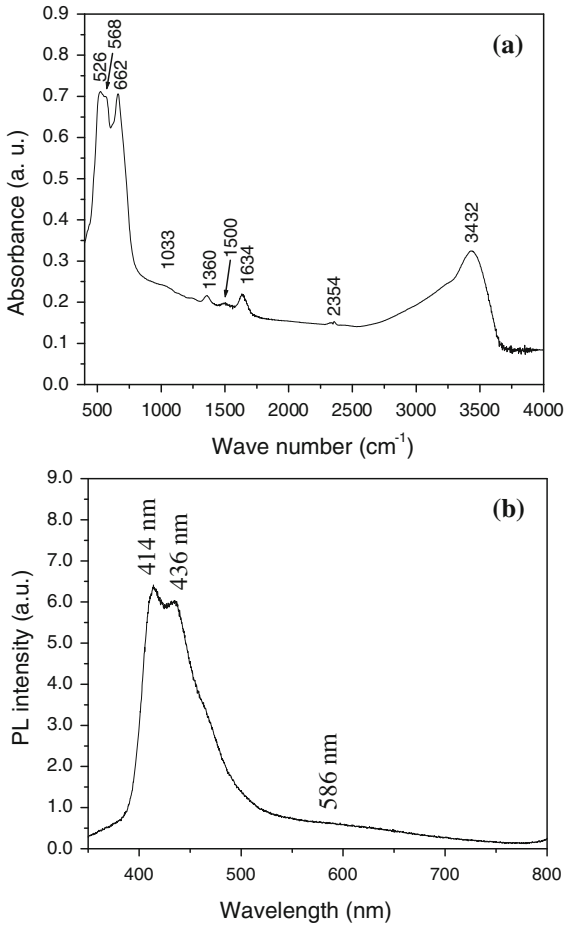

Fig. 7 Typical room temperature **a** FTIR and **b** PL spectra of the SnO_2 nanoparticles

2.84 eV, respectively. These two bands are frequently associated to the doubly ionized oxygen vacancies $\left(V_O^{++}\right)$ in SnO_2 (Das et al. 2006). The recombination of surface trapped hole with the electron at the deep trap level $\left(V_O^{+}\right)$ forms a doubly ionized oxygen vacancy center $\left(V_O^{++}\right)$. It is believed that the emissions are produced when an electron from the conduction band recombine with the holes at $\left(V_O^{++}\right)$ center (Seo et al. 2002). However, the most common emission associated with crystalline defects and stoichiometry deviation in SnO_2 is frequently observed in the visible spectral range (450–750 nm) (Cheng et al. 2004; Liu et al. 2003). As can be seen, there appeared a broad and very low-intensity emission band peaked around 586 nm (2.12 eV) in our samples, indicating their near-stoichiometric composition and excellent structural quality.

Conclusions

Synthesis of highly crystalline, 0-D and 1-D nanostructures of SnO_2 in quantum confinement regime could be possible in large scale by hydrothermal method controlling the pH of the reaction mixture and the temperature. While at lower pH values (pH 5–7) the spherical- or round-shaped SnO_2 nanoparticles grow through Ostwald ripening process of the small nuclei as growth units, and at higher pH values (pH > 9) uniform nanorods grow by oriented attachment process. Higher temperature of hydrothermal treatment accelerates the growth process and promotes the formation of longer 1-D structures. The results presented in this study demonstrate that by manipulating the pH of the reaction mixture, temperature, and time of hydrothermal treatment, surfactant-free SnO_2 nanoparticles of variable sizes and fine nanorods of desired lengths can be produced systematically.

Acknowledgments The work was partially supported by VIEP, BUAP (Project Grant VIEP/EXC/2012), and CONACyT, Mexico (Grant # 151767). The authors are thankful to L. Rendón and LCM, UNAM, Mexico for extending TEM facilities.

References

Alivisatos AP (1996) Perspectives on the physical chemistry of semiconductor nanocrystals. J Phys Chem 100:13226–13239

Ba J, Polleux J, Antonietti M, Niederberger M (2005) Non-aqueous synthesis of tin oxide nanocrystals and their assembly into ordered porous mesostructures. Adv Mater 17:2509–2512

Bhise AB, Dattatray J, Walke P, More MA, Mulla IS, Pillai VK, Joag DS (2007) A single In-doped SnO_2 submicrometre sized wire as a field emitter. J Phys D 40:3644–3646

Broussous L, Santilli CV, Pulcinelli SH, Craievich AF (2002) SAXS study of formation and growth of tin oxide nanoparticles in the presence of complexing ligands. J Phys Chem B 106:2855–2860

Cai D, Su Y, Chen Y, Jiang J, He Z, Chen L (2005) Synthesis and photoluminescence properties of novel SnO_2 asterisk-like nanostructures. Mater Lett 59:1984–1988

Carreño NLV, Nunes MR, Garcia ITS, Orlandi MO, Fajardo HV, Longo E (2009) Carbon-coated SnO_2 nanobelts and nanoparticles by single catalytic step. J Nanopart Res 11:955–963

Chen D, Gao L (2004) Novel synthesis of well-dispersed crystalline SnO_2 nanoparticles by water-in-oil microemulsion-assisted hydrothermal process. J Colloid Interface Sci 279:137–142

Chen YJ, Nie L, Xue XY, Wang YG, Wang TH (2006) Linear ethanol sensing of SnO_2 nanorods with extremely high sensitivity. Appl Phys Lett 88:083105

Cheng B, Russell JM, Shi W, Zhang L, Samulski ET (2004) Large-scale, solution-phase growth of single-crystalline SnO_2 nanorods. J Am Chem Soc 126:5972–5973

Chiu H-C, Yeh C-S (2007) Hydrothermal synthesis of SnO_2 nanoparticles and their gas-sensing of alcohol. J Phys Chem C 111:7256–7259

Dai ZR, Gole JL, Stout JD, Wang ZL (2002) Tin oxide nanowires, nanoribbons, and nanotubes. J Phys Chem B 106: 1274–1279

Das S, Kar S, Chaudhuri S (2006) Optical properties of SnO_2 nanoparticles and nanorods synthesized by solvothermal process. J Appl Phys 99:114303

de Monredon S, Cellot A, Ribot F, Sanchez C, Armelao L, Gueneau L, Delattre L (2002) Synthesis and characterization of crystalline tin oxide nanoparticles. J Mater Chem 12:2396–2400

Dieguez A, Romano Rodriguez A, Vila A, Morante JR (2001) The complete Raman spectrum of nanometric SnO_2 particles. J Appl Phys 90:1550

Escobedo-Morales A, Sánchez-Mora E, Pal U (2007) Use of diffuse reflectance spectroscopy for optical characterization of un-supported nanostructures. Rev Mex Fis S53: 18–22

Gu F, Wang SF, Lu MK, Zhou GJ, Yung DR (2004) Photoluminescence properties of SnO_2 nanoparticles synthesized by sol–gel method. J Phys Chem B 108:8119–8123

Hu JQ, Ma XL, Shang NG, Xie ZY, Wong NB, Lee CS, Lee ST (2002) Large-scale rapid oxidation synthesis of SnO_2 nanoribbons. J Phys Chem B 106:3823–3826

Hyeon T, Chung Y, Park J, Lee SS, Kim YW, Park BH (2002) Synthesis of highly crystalline and monodisperse cobalt ferrite nanocrystals. J Phys Chem B 106:6831–6833

Jain SC, Hughes AE (1978) Ostwald ripening and its application to precipitates and colloids in ionic crystals and glasses. J Mater Sci 13:1611–1631

Jiang LH, Sun GQ, Zhou ZH, Zhou WJ, Xin Q (2004) Preparation and characterization of PtSn/C anode electrocatalysts for direct ethanol fuel cell. Catal Today 93–95:665–666

Jiang L, Sun G, Zhou Z, Sun S, Wang Q, Yan S, Li H, Tian J, Guo J, Zhou B, Xin Q (2005) Size-controllable synthesis of monodispersed SnO_2 nanoparticles and application in electrocatalysts. J Phys Chem B 109:8774–8778

Jones FH, Dixon R, Foord JS, Egdell RG, Pethica JB (1997) The surface structure of $SnO_2(110)(4x1)$ revealed by scanning tunneling microscopy. Surf Sci 376:367–373

Kubelka P, Munk F (1931) Ein beitrag zur optik der farbanstriche. Z Tech Phys (Leipzig) 12:593–601

Lee JS, Sim SK, Min B, Cho K, Kim SW, Kim S (2004) Structural and optoelectronic properties of SnO_2 nanowires synthesized from ball-milled SnO_2 powders. J Crystal Growth 267:145–149

Lee EJH, Ribeiro C, Longo E, Leite ER (2006) Growth kinetics of tin oxide nanocrystals in colloidal suspensions under hydrothermal conditions. Chem Phys 328:229–235

Leite ER, Giraldi TR, Pontes FM, Longo E, Beltrán A, Andrés J (2003) Crystal growth in colloidal tin oxide nanocrystals induced by coalescence at room temperature. Appl Phys Lett 83:01566

Lifshitz JM, Slyozov SS (1961) The kinetics of precipitation from supersaturated solid solutions. J Phys Chem Solids 19:35–50

Liu Y, Zheng C, Wang W, Yin C, Wang G (2001a) Synthesis and characterization of rutile SnO_2 nanorods. Adv Mater 13:1883–1887

Liu YK, Zheng CL, Wang WZ, Zhan YJ, Wang GG (2001b) Production of SnO_2 nanorods by redox reaction. J Cryst Growth 233:8–12

Liu Z, Zhang D, Han S, Li C, Tang T, Jin W, Liu X, Lci B, Zhou C (2003) Laser ablation synthesis and electron transport studies of tin oxide nanowires. Adv Mater 15:1754–1757

Mädler L, Sahm T, Gurlo A, Grunwaldt JD, Barsan N, Weimar U, Pratsinis SE (2006) Sensing low concentrations of CO using flame-spray-made Pt/SnO_2 nanoparticles. J Nanopart Res 8:783–796

Merle P, Pascual J, Camassel J, Mathieu H (1980) Uniaxial-stress dependence of the first-order Raman spectrum of rutile. I. Experiments. Phys Rev B 21:01617–01626

Pan ZW, Dai ZR, Wang ZL (2001) Nanobelts of semiconducting oxides. Science 291:1947–1949

Pang G, Chen S, Koltypin Y, Zaban A, Feng S, Gedanken A (2001) Controlling the particle size of calcined SnO_2 nanocrystals. Nano Lett 1:723–726

Sangeetha P, Sasirekha V, Ramakrishnan V (2011) Micro-Raman investigation of tin dioxide nanostructured material based on annealing effect. J Raman Spectrosc 42:1634–1639

Seo HW, Bae SY, Park J, Yang H, Park KS, Kim S (2002) Strained gallium nitride nanowires. J Chem Phys 116: 9492–9499

Shao W, Wang Z, Zhang Y, Cui J, Yu W, Qian Y (2005) Controlled synthesis of SnO_2 hollow microspheres via a facile template-free hydrothermal route. Chem Lett 34:556–557

Shen E, Wang C, Wang E, Kang Z, Gao L, Hu C, Xu L (2004) PEG-assisted synthesis of SnO_2 nanoparticles. Mater Lett 58:3761–3764

Slater B, Catlow CRA, Gay DH, Williams DE, Dusastre V (1999) Study of surface segregation of antimony on SnO_2 surfaces by computer simulation techniques. J Phys Chem B 103:10644–10650

Sugimoto H, Tsukube H, Tanaka K (2004) Immobilization of a high-valent rhenium complex on an indium-doped tin-oxide electrode: enhanced catalytic activity of a trans-dioxorhenium(V) complex in electrochemical oxidation of alcohols. Eur J Inorg Chem 2004:4550–4553

Sun JQ, Wang JS, Wu XC, Zhang GS, Wei JY, Zhang SQ, Li H, Chen DR (2006) Novel method for high-yield synthesis of rutile SnO_2 nanorods by oriented aggregation. Cryst Growth Des 6:1584–1587

Wang Y, Jiang X, Xia Y (2003) A solution-phase, precursor route to polycrystalline SnO_2 nanowires that can be used for gas sensing under ambient conditions. J Am Chem Soc 125:16176–16177

Xu CK, Xu GD, Liu YK, Zhao XL, Wang GH (2002) Preparation and characterization of SnO_2 nanorods by thermal decomposition of SnC_2O_4 precursor. Scr Mater 46: 789–794

Xu G, Zhang YW, Sun X, Xu CL, Yan CH (2005) Synthesis, structure, texture, and CO sensing behavior of nanocrystalline tin oxide doped with scandia. J Phys Chem B 109:3269–3278

Xu X, Znuang J, Wang X (2008) SnO_2 quantum dots and quantum wires: controllable synthesis, self-assembled 2D

architectures, and gas-sensing properties. J Am Chem Soc 130:12527–12535

Yu S, Liu B, Mo M, Huang J, Liu X, Qian Y (2003) General synthesis of single-crystal tungstate nonorods/nanowires: a facile low-temperature solution approach. Adv Funct Mater 13:639–647

Zhang JR, Gao L (2004) Synthesis and characterization of nanocrystalline tin oxide by sol–gel method. J Solid State Chem 177:1425–1430

Zhang B, Tian Y, Zhang JX, Cai W (2011) Structural, optical, electrical properties and FTIR studies of fluorine doped SnO_2 films deposited by spray pyrolysis. J Mater Sci 46:1884–1889

Zhou JX, Zhang MS, Hong JM, Yin Z (2006) Raman spectroscopic and photoluminescence study of single-crystalline SnO_2 nanowires. Solid State Commun 138:242–246